

## Article

# Phase Diagrams of Polymerization-Induced Self-Assembly Are Largely Determined by Polymer Recombination

Artem Petrov <sup>1,\*</sup> , Alexander V. Chertovich <sup>1,2</sup>  and Alexey A. Gavrilov <sup>1,2</sup> <sup>1</sup> Faculty of Physics, Lomonosov Moscow State University, 119991 Moscow, Russia<sup>2</sup> Semenov Federal Research Center for Chemical Physics, 119991 Moscow, Russia

\* Correspondence: petrov.ai15@physics.msu.ru

**Abstract:** In the current work, atom transfer radical polymerization-induced self-assembly (ATRP PISA) phase diagrams were obtained by the means of dissipative particle dynamics simulations. A fast algorithm for determining the equilibrium morphology of block copolymer aggregates was developed. Our goal was to assess how the chemical nature of ATRP affects the self-assembly of diblock copolymers in the course of PISA. We discovered that the chain growth termination via recombination played a key role in determining the ATRP PISA phase diagrams. In particular, ATRP with turned off recombination yielded a PISA phase diagram very similar to that obtained for a simple ideal living polymerization process. However, an increase in the recombination probability led to a significant change of the phase diagram: the transition between cylindrical micelles and vesicles was strongly shifted, and a dependence of the aggregate morphology on the concentration was observed. We speculate that this effect occurred due to the simultaneous action of two factors: the triblock copolymer architecture of the terminated chains and the dispersity of the solvophobic blocks. We showed that these two factors affected the phase diagram weakly if they acted separately; however, their combination, which naturally occurs during ATRP, affected the ATRP PISA phase diagram strongly. We suggest that the recombination reaction is a key factor leading to the complexity of experimental PISA phase diagrams.

**Keywords:** block-copolymer micelles; polymerization-induced self-assembly; ATRP; computer simulations; dissipative particle dynamics



**Citation:** Petrov, A.; Chertovich, A.V.; Gavrilov, A.A. Phase Diagrams of Polymerization-Induced Self-Assembly Are Largely Determined by Polymer Recombination. *Polymers* **2022**, *14*, 5331. <https://doi.org/10.3390/polym14235331>

Academic Editor: Shin-Ichi Yusa

Received: 17 October 2022

Accepted: 28 November 2022

Published: 6 December 2022

**Publisher's Note:** MDPI stays neutral with regard to jurisdictional claims in published maps and institutional affiliations.



**Copyright:** © 2022 by the authors. Licensee MDPI, Basel, Switzerland. This article is an open access article distributed under the terms and conditions of the Creative Commons Attribution (CC BY) license (<https://creativecommons.org/licenses/by/4.0/>).

## 1. Introduction

Block copolymers are able to self-assemble in selective solvents; the typical morphologies observed in such systems include vesicles as well as spherical and cylindrical micelles. These aggregates can serve as nanoreactors and as imaging and drug delivery systems [1]. Block copolymer micelles and vesicles can be obtained by synthesizing block copolymers in a good solvent and adding a cosolvent that is poor for one of the blocks afterwards. This method of preparation of the block copolymer aggregates has a serious drawback: the addition of the cosolvent leads to a low concentration of the polymer product, typically less than 1% [2–4]. This problem is one of the key reasons for the limited implementation of block copolymer self-assembly in the industry [2–4].

One of the recently developed ways to overcome this challenge is to synthesize block copolymers directly in a selective solvent. Typically, the corona-forming block (A-block) is presynthesized and placed in a good solvent mixed with monomers for the core-forming block (B-block). The B-block monomers are chosen in such a way that they are soluble in the nonpolymerized state and nonsoluble when they form a polymer chain. Therefore, block copolymers appear in the selective solvent during the B-block synthesis, and thus are able to self-assemble without addition of cosolvents. Such a method of producing block copolymer aggregates is called dispersion polymerization-induced self-assembly (PISA) [3,5]. The concentration of the polymer product after PISA can reach 10–50%, a value

that is an order of magnitude larger than that typical for the traditional method of cosolvent addition to presynthesized copolymers [2,5].

Usually, PISA is conducted using reversible deactivation radical polymerization (RDRP) techniques such as reversible addition–fragmentation chain-transfer (RAFT) [3,5,6], atom transfer radical polymerization (ATRP) [7–9], or nitroxide-mediated polymerization (NMP) [10–12]. Further, we focus on the case of ATRP PISA due to its popularity and the relative simplicity for its modeling compared to the RAFT PISA [13].

ATRP is more complex than living anionic polymerization from the standpoint of the chemical kinetics. First, ATRP includes the reaction of reversible activation–deactivation of the growing ends of polymer chains. Second, chain termination is present during ATRP in contrast to the anionic polymerization. At the same time, ATRP PISA phase diagrams feature significant complexity: they include multiple phase coexistence regions and exhibit a strong dependence of the aggregate morphology on the polymer concentration [8]. It is possible that the complexity of the ATRP kinetics induces the complexity of the ATRP PISA phase diagrams. First of all, termination via recombination leads to the formation of ABA triblock copolymers; since the polymer architecture may influence self-assembly [14,15], the presence of a termination via recombination may also affect the morphology of the ATRP PISA aggregates. Second, the rates of the reversible activation/deactivation and termination reactions relative to the rate of the propagation affect the polymer dispersity, and it is known that the dispersity can influence the process of the block copolymer's self-assembly [16–20]. These considerations point out that it should be possible to control the morphology of ATRP PISA aggregates by controlling the kinetics of ATRP. However, the influence of different reactions occurring during ATRP on the ATRP PISA phase diagrams has been studied very poorly.

As it is very hard to discern between different factors affecting PISA phase diagrams in experiments, computer simulations can be employed to gain an insight into this complex problem. There exist several works on simulating the process of PISA [21–25]; however, those studies considered the simplest polymerization scheme that included only initiation and propagation reactions without chain activation–deactivation and termination reactions. In fact, the previous works modeled RDRP as an ideal living polymerization. As a result, the dispersity after PISA was significantly lower than typically observed in experiments [21,24]. Moreover, the absence of recombination in the previous models of polymerization led to the formation of only diblock copolymers during PISA. In those works, the influence of the presence of triblock copolymers on PISA phase diagrams was not studied. To the best of our knowledge, no attempt has been made to model PISA with a realistic polymerization scheme resembling the real process of RDRP.

In this work, we used the dissipative particle dynamics (DPD) technique [26–30] to simulate the process of ATRP PISA. In our model, we took into account the essential reactions occurring during ATRP. We assessed how the reversible activation–deactivation reaction and the reaction of termination via recombination affected the PISA phase diagrams. The former reaction led to an increase in the polymer dispersities up to 1.2; similar values are experimentally observed in well-controlled PISA [3,31]. However, despite this increase in the dispersity, ATRP PISA without the termination reaction yielded almost the same phase diagram as PISA modeled by an ideal living polymerization. On the other hand, termination affected the phase diagram strongly, shifting the transition between cylindrical micelles and vesicles and giving rise to a strong dependence of the aggregate morphology on concentration, which is typically observed in experiments. We believe that recombination is one of the key chemical processes affecting ATRP PISA.

## 2. Methods

To perform simulations, dissipative particle dynamics [26–30] (DPD) was utilized. DPD is a mesoscale molecular dynamics technique with a soft conservative force and explicit solvent. This method is well-suited for simulating polymer systems on a coarse-grained level. Macromolecules were modeled by the bead-and-spring model, with beads

interacting by a conservative force (repulsion)  $F_{ij}^c$ , a bond stretching force (only for connected beads)  $F_{ij}^b$ , a dissipative force (friction)  $F_{ij}^d$ , and a random force (heat generator)  $F_{ij}^r$ . The total force was given by:  $F_i = \sum_{i \neq j} (F_{ij}^c + F_{ij}^b + F_{ij}^d + F_{ij}^r)$ . The soft-core repulsion between the  $i$ th and the  $j$ th beads was equal to:

$$F_{ij}^c = \begin{cases} a_{\alpha\beta} \left(1 - \frac{r_{ij}}{R_{cut}}\right) \frac{\mathbf{r}_{ij}}{r_{ij}}, & r_{ij} \leq R_{cut}, \\ 0, & r_{ij} > R_{cut}. \end{cases} \quad (1)$$

Here,  $\mathbf{r}_{ij}$  is the vector between the  $i$ th and the  $j$ th bead,  $a_{\alpha\beta}$  is the repulsion parameter if the bead  $i$  has the type  $\alpha$  and the bead  $j$  has the type  $\beta$ , and  $R_{cut}$  is the cutoff distance.  $R_{cut}$  is usually taken as the length scale, i.e.,  $R_{cut} = 1$  [30]. In the present work,  $a_{\alpha\alpha} = 25$  was used ( $a_{\alpha\alpha}$  represents the interaction parameters between alike beads, i.e., when  $\beta = \alpha$ ). In that case, the interaction parameters  $a_{\alpha\beta}$  and a more common Flory–Huggins parameter  $\chi$  are linearly related to each other [30]:  $a_{\alpha\beta} = \chi/0.306 + 25$ ,  $\alpha \neq \beta$ . If two beads ( $i$  and  $j$ ) are connected by a bond, there is also a simple spring force acting on them:  $F_{ij}^b = -K(r_{ij} - l_0)\mathbf{r}_{ij}/r_{ij}$ , where  $K$  is the bond stiffness and  $l_0$  is the equilibrium bond length. The following set of parameters was used to simulate bonds:  $K = 4$ ,  $l_0 = 0$ . A more detailed description and parameters discussion of the standard DPD scheme can be found elsewhere [26–30,32].

The ATRP reaction was modeled as described in ref. [32]. The algorithm is shown schematically in Figure 1. During polymerization, two beads could form a permanent bond when they were located closer than  $R_{cut} = 1.0$  (i.e., when they were close enough to start interacting through the volume potential) from each other in space (the details of this procedure are given in refs. [21,32]). The reaction routine was run every  $N_{stp} = 200$  DPD time steps. This number was large enough to ensure local equilibration of the system between consequent reaction routine runs, and small enough to result in a continuous reaction process. In the reaction routine, bonds could be formed with a certain probability depending on the type of reaction. Our systems contained three types of beads: A-type beads (solvophilic blocks, macroinitiators), B-type beads (solvophobic monomers and monomer units), and solvent (S). The initial system state was a homogeneous mixture of macroinitiators, solvent, and nonpolymerized B-type monomers. A single macroinitiator was formed by six A-type beads; the end of the chain  $A^*$  could form a bond (Figure 1). The  $A^*$  beads were in the dormant state with a probability  $p_{A,dorm} = 0.99$ ; in this state, the  $A^*$  beads were unable to form bonds (i.e., they were treated as nonreactive). When an  $A^*$  bead was not in the dormant state, it was able to form a bond with a B-type bead with a probability  $p_i = 0.999$ ; this B-type bead started to form the B-block. B-type beads at the ends of growing B-blocks ( $B^*$ ) were in the dormant state with a probability  $p_{B,dorm} = 0.9$ . In the active state, a B-type bead at the end of a B-block ( $B^*$ ) could form a bond with a nonpolymerized B-type bead with a probability  $p_p = 0.05$ . It is worth mentioning that in the present work, a generalized coarse-grained model of ATRP was utilized, and the transition metal catalyst was not simulated explicitly. Instead, its presence was taken into account implicitly in the activation/deactivation of the growing chains as a reversible change of the state (dormant/active) of the end-bead of the chains.

For simplicity, termination proceeded only via recombination: nondormant  $A^*$  or  $B^*$  ends of two polymer chains could form a bond with a probability  $p_t$  if they were located closer than  $R_{cut}$  to each other. In this work, we adjusted  $p_t$  to investigate the self-assembly close to  $\approx 100\%$  conversion for the following three cases: (i) no recombination ( $p_t = 0$ ), i.e. only diblock copolymers were formed in the system; (ii) recombination is present, and  $\approx 50\%$  of chains underwent recombination; and (iii) recombination is present, and  $\approx 95\%$  of all chains were terminated. Case (ii) can in general be considered as a simplified model of a more realistic ATRP PISA process, in which recombination via both recombination and disproportionation is present. For case (iii), the value of  $p_t$  was fixed at 0.05, while for case (ii), it was adjusted to achieve the target fraction of terminated chains ( $\approx 50\%$ ) at a high conversion degree.

The values of the aforementioned reaction probabilities were chosen so that the molecular weight distributions (MWDs) (i) had experimentally reasonable dispersities for  $p_t = 0$  (no recombination) and (ii) were unimodal, i.e., had a single peak at all conversions (Figure 2). Typical dispersities achieved in the systems without recombination ( $p_t = 0$ ) were around 1.1–1.2 at 100% conversion (Figures 2 and S2). When the reaction probabilities were adjusted in an attempt to further widen the distributions, the second peak started to appear in MWDs at high polymer volume fractions and low  $N_B/N_A$  values.

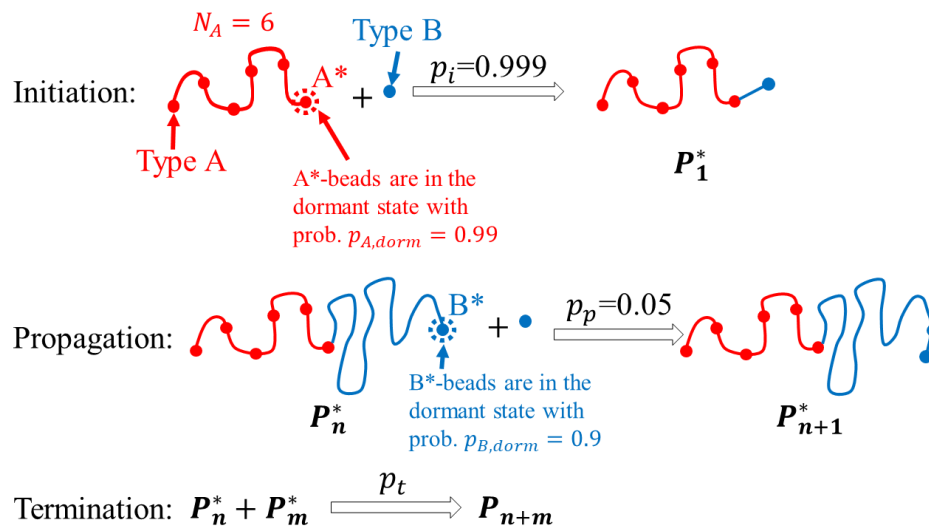


Figure 1. Algorithm of the ATRP simulation.

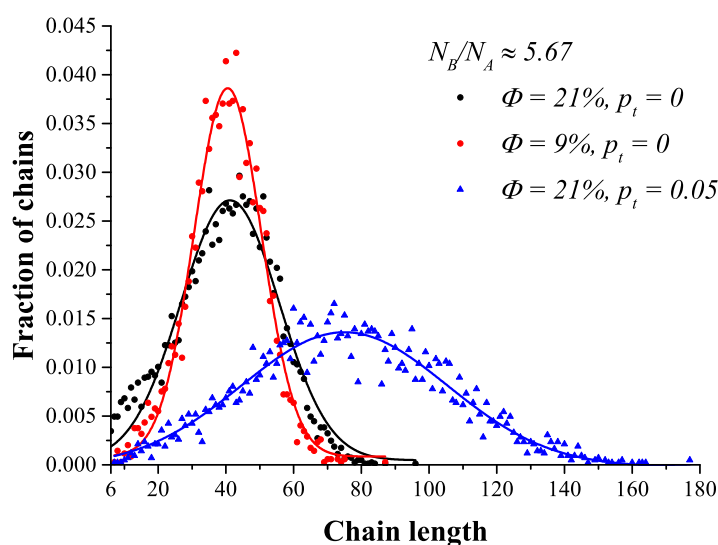


Figure 2. Molecular weight distributions of the modeled systems at a fixed chain composition ( $N_A = 6$ ,  $N_B = 34$ ) at different polymer volume fractions  $\Phi$  and termination probabilities  $p_t$  at 100% conversion; 95% of the chains in the system with  $p_t = 0.05$  underwent termination. Dispersities (values of  $M_w/M_n$ ) are equal to 1.13, 1.07, and 1.14 for the black, red, and blue curves, respectively.

The Flory–Huggins parameters  $\chi$  of all interactions were equal to zero except for the interaction between the A-type beads and B-type beads ( $\chi_{AB}$ ) and between the solvent and B-type beads ( $\chi_{SB}$ ). We set  $\chi_{AB} = \chi_{SB} = 1.9$  as in ref. [21]: such choice ensured poor solvent conditions for the growing chains but did not lead to the precipitation of the nonpolymerized B-type beads. All bond potential and conservative force coefficients were set to make phantom chains for faster equilibration as described in ref. [21]. In our simulations, we used a cubic simulation box with periodic boundary conditions with a size

of  $80 \times 80 \times 80$  DPD units. The total number of beads in one system was equal to  $1.536 \times 10^6$  (DPD density  $\rho = 3$ ); such a large size of the simulation box was chosen to reduce the influence of the finite-size effects. The integration timestep was equal to  $\Delta t = 0.04$ .

To verify that the ATRP simulation algorithm described above modeled ATRP realistically, we analyzed the molecular weight distributions (MWDs) in the systems with a nonzero recombination probability at different polymer concentrations and compositions (Figure 2; see also Supplementary Materials, Section S1). The data in Figures 2 and S1 (black lines) show that MWDs were unimodal (as in the majority of experiments [8,9,33,34]). Moreover, our data suggest that the MWDs from our simulations changed with the polymer concentration and composition (Figure S1). In addition, we chose the reaction probabilities to speed up the calculations of ATRP; as a result, the ratios of the reaction probabilities did not correspond to the values typical for experimental systems. However, we additionally tested the reaction probabilities ratios closer to the experimental ones and did not observe any significant differences in the MWDs. Therefore, we believe that it is unlikely that our results were influenced by this choice of elevated reaction probabilities (see Supplementary Materials, Section S1).

After devising a computationally efficient way to simulate ATRP, we calculated the ATRP PISA phase diagrams. However, polydisperse polymers having different architectures due to recombination self-assemble into thermodynamically equilibrium structures very slowly. To overcome this challenge, we developed a fast algorithm of the phase diagram calculation (Supplementary Materials, Section S2). The fast algorithm consisted of the following three stages: (i) ATRP polymerization until 100% conversion was reached and the needed number of chains underwent recombination; (ii) precipitation of the chains into a single aggregate; and (iii) transformation of the aggregate into an equilibrium morphology. The phase diagrams for PISA without recombination (only diblock copolymers present in the system) were calculated both by the fast algorithm and by natural system evolution, and these two phase diagrams coincided (Figure S3). Given that the morphology equilibration essentially started from two very distinct initial states (i.e., precipitated and homogeneous) but the resulting morphologies were the same, we believe that the equilibrium phase diagrams were obtained. Moreover, this validation of the fast algorithm suggested that it could be used on its own to obtain equilibrium phase diagrams. Thus, the phase diagrams for ATRP PISA with recombination were calculated only via the fast algorithm, since it was very hard to obtain the equilibrium morphologies by natural evolution in a feasible time due to the very slow system relaxation (presumably because of the presence of triblock copolymers).

### 3. Results and Discussion

#### 3.1. ATRP without Recombination

First, we studied the process of ATRP PISA without recombination ( $p_t = 0$ ). We obtained phase diagrams at 100% conversion, i.e., all B-type monomers were polymerized. The studied polymer volume fractions were 9%, 13%, 17%, and 21%. The phase diagram for this process is shown in Figure 3a.

In the phase diagram, three regions were observed: (i) a region of coexistence of spherical (sph) and cylindrical (cyl) micelles (similarly to our previous work [21]); (ii) pure cylindrical micelles; and (iii) vesicles (ves). We did not observe the regions of coexistence between the last two morphologies: there was a single transition line, almost independent of the concentration (Figure 3a). In the present work, we did not study the transition between the sph+cyl region and the region of pure spherical micelles that should occur at smaller values of  $N_B/N_A$ . We obtained the position of the sph+cyl $\leftrightarrow$ cyl transition, and it was found to be almost the same as in [21]. Due to some ambiguity in the determination of the position of that transition, we mostly focused on the cylinders–vesicles transition (Figure 3b). To assess the influence of the ATRP-specific chemical reactions on the ATRP-induced self-assembly, we compared our data with two reference phase diagrams: (i) the self-assembly of monodisperse diblock copolymers and (ii) the self-assembly induced

by living polymerization. Living polymerization was modeled by only two reactions: initiation and propagation, and no dormant chains were present. The reference phase diagrams were obtained in our previous work [21]. From Figure 3b, one can clearly see that the cylinders–vesicles transition line for ATRP PISA with no termination was shifted to higher values of B-block lengths compared to the two reference diagrams (Figure 3b). This phenomenon may be explained by an increase in the B-block dispersity: systems with more polydisperse B-blocks were shown to yield phase diagrams with a shifted line of transition between cylinders and vesicles [21]. Since the reversible activation–deactivation (i.e., the presence of dormant chains) led to an increase in the B-block dispersity compared to living polymerization in all systems (Figure S2b), the aforementioned transition line was shifted to higher values of B-block lengths in the case of ATRP PISA. This shift was notable compared to the system of monodisperse diblock copolymers but was much less significant in comparison with the living PISA (Figure 3b). These data suggest that chemical reactions specific to ATRP do not have a strong influence on the PISA phase diagrams in the absence of recombination.

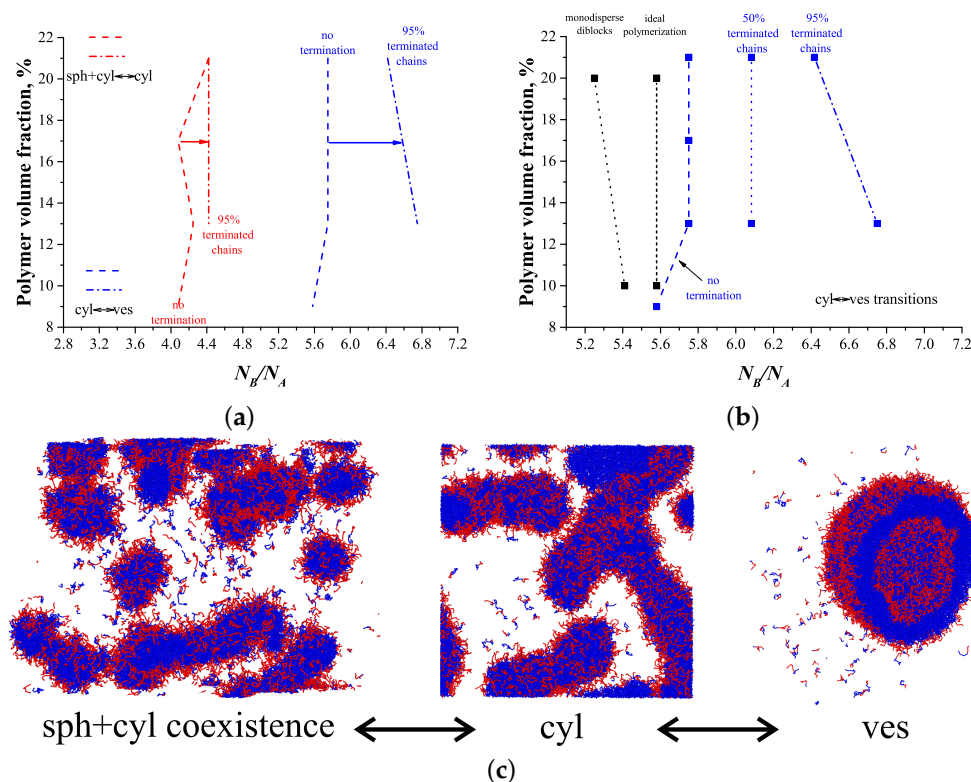


**Figure 3.** (a) Phase diagram for the systems without recombination ( $p_t = 0$ , transition lines are dashed) and for the systems with the fraction of terminated chains via recombination equal to  $\approx 95\%$  ( $p_t = 0.05$ , transition lines are dash-dotted). Sph+cyl and cyl regions are to the left and to the right side of the red lines, respectively. Cyl and ves regions are to the left and to the right side of the blue lines, respectively. (b) Transition lines between cylinders and vesicles for the systems with different fractions of terminated chains. Squares show the simulation data. Transition points for the reference systems (monodisperse diblock copolymers and ideal polymerization PISA at 10% and 20%) were obtained in ref. [21] and are shown in black. The cyl $\leftrightarrow$ ves transition points were tested in three independent runs for the systems with 95% of terminated chains. (c) Snapshots of the observed morphologies.

### 3.2. ATRP with Recombination

Next, we studied the self-assembly in the systems with nonzero recombination probabilities. We started with the case of  $\approx 95\%$  terminated chains; since only recombination was considered, those chains formed ABA triblock copolymers. The examples of molecular

weight distributions for such systems are shown in Figures 2 and S1. After reaching 100% conversion and 95% fraction of recombined chains, we stopped the reaction and studied the self-assembly behavior in the systems; the cyl $\leftrightarrow$ ves transition points were tested in three independent runs. The phase diagram is shown in Figure 3a,b. The transition between cylinders and vesicles occurred at much larger  $N_B/N_A$  values than in the systems with no termination. Moreover, we observed a pronounced dependency of aggregate morphology on concentration in the  $\approx 95\%$  terminated chains case.

To find out the reasons for such behavior, we carried out simulations of the self-assembly of monodisperse ABA triblock copolymers (Figure S4). To our surprise, we found that the transition between cylindrical micelles and vesicles occurred at very similar  $N_B/N_A$  values as in the case of monodisperse diblock copolymers. Therefore, the architecture of monodisperse block copolymers alone did not affect the transition between cylindrical micelles and vesicles strongly.

Further, we compared the dispersities of the B-blocks in the systems with no recombination and with  $\approx 95\%$  terminated chains. We discovered that at  $\Phi = 21\%$ , the recombination reaction affected the B-block dispersity weakly. For example, for the systems with  $N_B/N_A \approx 6.3$ , the B-block dispersity increased from 1.15 (no termination) to 1.18 ( $\approx 95\%$  terminated chains). At  $\Phi = 13\%$ , for the systems with  $N_B/N_A \approx 6.3$ , the B-block dispersity increased from 1.11 to 1.2 after increasing the fraction of terminated chains from 0% to  $\approx 95\%$ . This increase in the B-block dispersity was approximately equal to the difference of chain dispersities between the ideal living polymerization [21] and ATRP without termination (Figure S2b); however, the two latter processes yielded very close phase diagrams (Figure 3b). Hence, the only explanation for the dramatic change of the phase diagram after taking into account the recombination reaction is that the B-block dispersity affects the self-assembly of ABA triblock and AB diblock copolymers somehow differently. In particular, we suggest that cylinders formed by ABA triblock copolymers are much more susceptible to changes in the B-block dispersity than those formed by AB diblock copolymers.

This fact also explains the strong concentration dependence of the cylinder–vesicle transition (Figure 3b). This dependence arises due to the slight changes of B-block dispersity, and not due to the change of polymer concentration itself; simulations described in Supplementary Materials, Section S4, substantiate this hypothesis.

Figure 4 provides a qualitative explanation of the phenomenon described above by comparing the packing of polymer chains in the cylindrical micelles. We suppose that there are two qualitatively different conformations of an ABA triblock copolymer in a micelle. To form a conformation of the first type, the two A-blocks reside in close proximity to each other in the corona of the micelle, and a B-block forms a “loop” close to the core–corona interface. The copolymer chains having the second type of conformations go through the micelle, having A-blocks on the opposite sides of the micelle. Obviously, the second type of conformations can be realized only by long enough chains. An increase in the B-block dispersity leads to a widening of the B-block length distribution, introducing more blocks with higher lengths, which are able to go through the micelle’s core center. We believe that this type of conformations stabilizes cylindrical (i.e., more curved) micelles, since it allows the system to reduce the entropy losses due to the redistribution of the blocks of different lengths in the micelle core, with longer blocks occupying the center. As a result, higher  $N_B/N_A$  values are needed to form a vesicle compared to less polydisperse systems. There have been experimental evidences of such “separation” of the core-forming blocks of different lengths in the cores of diblock copolymer micelles [35]; however, owing to two A blocks which reside in the corona and the subsequent conformational peculiarities of the core-forming B-blocks, triblock copolymers seem to be more sensible to changes in the B-block dispersity compared to diblock copolymers.

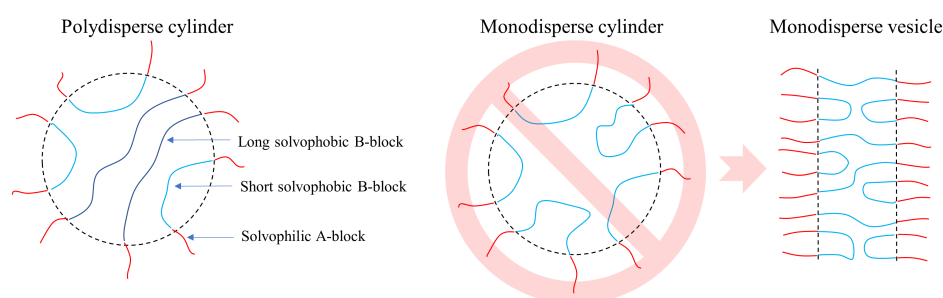


**Figure 4.** Schematic representation of the packing of ABA triblock copolymers inside micelles.

To characterize the chain packing inside the micelles in a more quantitative manner, we compared two systems at a fixed value of  $N_B/N_A \approx 6.67$  and polymer volume fraction of  $\Phi = 21\%$ . One of these systems was obtained by the usual ATRP PISA approach with the fraction of terminated chains equal to 95% (in this system, the dispersity of the B-block of the ABA triblock copolymers was equal to 1.17), while the other was obtained by removing part of the solvent from the corresponding system at  $\Phi = 13\%$  as described in Section S5 of the Supplementary Materials (in this system, the dispersity of the B-block of the ABA triblock copolymers was equal to 1.23). In the former system, vesicles were obtained (Figure 3b), while in the latter system, cylinders were observed (Figure S5). We compared the distributions of the end-to-end distances of the central B-blocks of the ABA triblock copolymers in these two systems; the chain ensemble forming the cylinder had more chains having larger end-to-end distances (Section S5, Figure S6). This supported our hypothesis that the shape of the MWD influenced the micelles morphology through the chain packing.

The self-assembly behavior of systems with intermediate fraction ( $\approx 50\%$ ) of terminated chains corroborated the aforementioned arguments (Figure 3b). To prepare such systems, we chose  $p_t = 0.0215$  at  $\Phi = 21\%$  and  $p_t = 0.015$  at  $\Phi = 13\%$ ; two different termination probabilities were chosen to avoid bimodal molecular weight distributions and to reach high conversions ( $\approx 98\%$ ). The reaction was stopped when 50% of the chains were terminated, and the self-assembly behavior was studied afterwards. Figure 3b demonstrates that the transition line between cylinders and vesicles for  $\approx 50\%$  terminated chains lies in between the transition lines for the systems with no termination and with  $\approx 95\%$  terminated chains. This is expected from our qualitative picture explaining the different effect the B-block dispersity has on the transition (Figure 4).

#### 4. Conclusions

In our work, we developed a DPD-based model of ATRP PISA that reproduced the key elements of the ATRP chemical reaction. We demonstrated that the termination via recombination strongly affected ATRP PISA phase diagrams; presumably, this happened because of the enhanced influence of the B-block dispersity on the self-assembly of ABA triblock copolymers. Due to this effect, ATRP PISA with recombination yielded phase diagrams that had a strong dependence of the aggregate morphology on the polymer concentration similar to experiments.

Qualitatively, our findings are in agreement with existing experimental data. For example, in some studies on ATRP PISA [8,36] it was observed that wormlike micelles could turn into vesicles upon an increase in the polymer concentration at a fixed composition. One of the main results of our work agrees well with these data: the introduction of a high fraction of chains terminated via recombination leads to a tilted cyl-ves transition line. Namely, for certain  $N_B/N_A$  values, we observed cylindrical micelles at  $\Phi = 13\%$  and vesicles at  $\Phi = 21\%$  (Figure 3b). At low fractions of chains terminated via recombination, the cyl-ves transition lines were almost vertical (i.e., there was no dependence of the morphology on the polymer concentration); therefore, we can speculate that recombination is one of the key factors controlling the micelles' morphology in the real PISA process.

**Supplementary Materials:** The following supporting information can be downloaded at: <https://www.mdpi.com/article/10.3390/polym14235331/s1>. Figure S1. Molecular weight distributions (MWDs) in various studied systems at different polymer volume fractions  $\Phi$  and different values of  $N_B/N_A$ . Black lines represent MWDs in the systems simulated according to the procedure described in the main text ( $p_t = 0.05$ , 95% of all chains terminated). Red lines represent MWDs in the systems with "slow" chemical reactions. Figure S2. Dispersity of chains as a function of  $N_B/N_A$  values at 100% conversion ( $p_t = 0$ ). Black dots - dispersities achieved during PISA induced by ideal living polymerization at 100% conversion. Figure S3. Comparison of the phase diagrams of ATRP PISA without recombination ( $p_t = 0$ ) obtained by the fast algorithm (dots) and by the natural system evolution (black rectangles). Red dots represent the state of coexistence between spherical and cylindrical micelles, blue dots show the state of pure cylindrical micelles, and green dots represent vesicles. Black rectangles show the points of transition determined by long enough simulations of natural system evolution. Figure S4. Comparison of the lines of transition between cylindrical micelles and vesicles for monodisperse ABA-triblock-copolymers and AB-diblock-copolymers. Figure S5. Points of transition between cylindrical micelles and vesicles for the systems with  $\approx 95\%$  of terminated chains. Blue dashed-dotted line shows the cylinder-vesicle transition line in the original simulation (Figure 3b in the main text). Blue arrow shows how the transition point shifted after the process of solvent removal described above. Figure S6. Comparison of the distributions of the end-to-end distances of the central B-blocks of the ABA-triblock-copolymers in the systems at a fixed value of  $N_B/N_A = 6.67$  and  $\Phi = 21\%$ . The vesicle is obtained during standard ATRP PISA routine, while the cylinder was obtained by the solvent removal procedure. Inset shows the same distribution, but for the volume fraction of B blocks instead of the number fraction. References [21,37] are cited in the supplementary materials.

**Author Contributions:** Conceptualization, A.V.C. and A.A.G.; methodology, A.P. and A.A.G.; software, A.A.G.; validation, A.P. and A.A.G.; formal analysis, A.P. and A.A.G.; investigation, A.P.; writing—original draft preparation, A.P.; writing—review and editing, A.P., A.A.G. and A.V.C.; visualization, A.P. and A.A.G.; supervision, A.A.G.; project administration, A.V.C.; funding acquisition, A.V.C. All authors have read and agreed to the published version of the manuscript.

**Funding:** This research was funded by the Russian Science Foundation project 19-73-20030.

**Data Availability Statement:** The data that support the findings of this study are available from the corresponding author upon reasonable request.

**Acknowledgments:** The research was performed using the equipment of the shared research facilities of HPC computing resources at Lomonosov Moscow State University. Artem Petrov is also acknowledge the personal fellowship of Interdisciplinary Scientific and Educational School of Moscow University "Photonic and Quantum technologies. Digital medicine".

**Conflicts of Interest:** The authors declare no conflict of interest.

## References

1. Mai, Y.; Eisenberg, A. Self-assembly of block copolymers. *Chem. Soc. Rev.* **2012**, *41*, 5969–5985. [[CrossRef](#)] [[PubMed](#)]
2. Cao, J.; Tan, Y.; Chen, Y.; Zhang, L.; Tan, J. Expanding the Scope of Polymerization-Induced Self-Assembly: Recent Advances and New Horizons. *Macromol. Rapid Commun.* **2021**, *42*, 2100498. [[CrossRef](#)] [[PubMed](#)]
3. Blanazs, A.; Madsen, J.; Battaglia, G.; Ryan, A.J.; Armes, S.P. Mechanistic insights for block copolymer morphologies: How do worms form vesicles? *J. Am. Chem. Soc.* **2011**, *133*, 16581–16587. [[CrossRef](#)]
4. Tritschler, U.; Pearce, S.; Gwyther, J.; Whittell, G.R.; Manners, I. 50th anniversary perspective: Functional nanoparticles from the solution self-assembly of block copolymers. *Macromolecules* **2017**, *50*, 3439–3463. [[CrossRef](#)]
5. Sugihara, S.; Blanazs, A.; Armes, S.P.; Ryan, A.J.; Lewis, A.L. Aqueous dispersion polymerization: A new paradigm for in situ block copolymer self-assembly in concentrated solution. *J. Am. Chem. Soc.* **2011**, *133*, 15707–15713. [[CrossRef](#)]
6. Warren, N.J.; Mykhaylyk, O.O.; Mahmood, D.; Ryan, A.J.; Armes, S.P. RAFT aqueous dispersion polymerization yields poly(ethylene glycol)-based diblock copolymer nano-objects with predictable single phase morphologies. *J. Am. Chem. Soc.* **2014**, *136*, 1023–1033. [[CrossRef](#)]
7. Wan, W.M.; Pan, C.Y. Atom transfer radical dispersion polymerization in an ethanol/water mixture. *Macromolecules* **2007**, *40*, 8897–8905. [[CrossRef](#)]
8. Wang, G.; Schmitt, M.; Wang, Z.; Lee, B.; Pan, X.; Fu, L.; Yan, J.; Li, S.; Xie, G.; Bockstaller, M.R.; et al. Polymerization-induced self-assembly (PISA) using ICAR ATRP at low catalyst concentration. *Macromolecules* **2016**, *49*, 8605–8615. [[CrossRef](#)]

9. Wang, K.; Wang, Y.; Zhang, W. Synthesis of diblock copolymer nano-assemblies by PISA under dispersion polymerization: Comparison between ATRP and RAFT. *Polym. Chem.* **2017**, *8*, 6407–6415. [[CrossRef](#)]
10. Groison, E.; Brusseau, S.; D'Agosto, F.; Magnet, S.; Inoubli, R.; Couvreur, L.; Charleux, B. Well-defined amphiphilic block copolymer nanoobjects via nitroxide-mediated emulsion polymerization. *ACS Macro Lett.* **2012**, *1*, 47–51. [[CrossRef](#)] [[PubMed](#)]
11. Qiao, X.; Lansalot, M.; Bourgeat-Lami, E.; Charleux, B. Nitroxide-Mediated Polymerization-Induced Self-Assembly of Poly (poly (ethylene oxide) methyl ether methacrylate-co-styrene)-b-poly (n-butyl methacrylate-co-styrene) Amphiphilic Block Copolymers. *Macromolecules* **2013**, *46*, 4285–4295. [[CrossRef](#)]
12. Qiao, X.; Dugas, P.Y.; Charleux, B.; Lansalot, M.; Bourgeat-Lami, E. Nitroxide-mediated polymerization-induced self-assembly of amphiphilic block copolymers with a pH/temperature dual sensitive stabilizer block. *Polym. Chem.* **2017**, *8*, 4014–4029. [[CrossRef](#)]
13. Gavrilov, A.A.; Chertovich, A.V. Simulation of the RAFT polymerization in 3D: Steric restrictions and incompatibility between species. *Polym. Chem.* **2022**, *13*, 2143–2154. [[CrossRef](#)]
14. Cai, D.; Li, J.; Ma, Z.; Gan, Z.; Shao, Y.; Xing, Q.; Tan, R.; Dong, X.H. Effect of Molecular Architecture and Symmetry on Self-Assembly: A Quantitative Revisit Using Discrete ABA Triblock Copolymers. *ACS Macro Lett.* **2022**, *11*, 555–561. [[CrossRef](#)]
15. Huo, M.; Xu, Z.; Zeng, M.; Chen, P.; Liu, L.; Yan, L.T.; Wei, Y.; Yuan, J. Controlling vesicular size via topological engineering of amphiphilic polymer in polymerization-induced self-assembly. *Macromolecules* **2017**, *50*, 9750–9759. [[CrossRef](#)]
16. Terreau, O.; Luo, L.; Eisenberg, A. Effect of poly (acrylic acid) block length distribution on polystyrene-b-poly (acrylic acid) aggregates in solution. 1. Vesicles. *Langmuir* **2003**, *19*, 5601–5607. [[CrossRef](#)]
17. Terreau, O.; Bartels, C.; Eisenberg, A. Effect of poly (acrylic acid) block length distribution on polystyrene-b-poly (acrylic acid) block copolymer aggregates in solution. 2. A partial phase diagram. *Langmuir* **2004**, *20*, 637–645. [[CrossRef](#)]
18. Gao, Z.; Eisenberg, A. A model of micellization for block copolymers in solutions. *Macromolecules* **1993**, *26*, 7353–7360. [[CrossRef](#)]
19. Linse, P. Micellization of poly (ethylene oxide)-poly (propylene oxide) block copolymers in aqueous solution: Effect of polymer polydispersity. *Macromolecules* **1994**, *27*, 6404–6417. [[CrossRef](#)]
20. Jiang, Y.; Chen, T.; Ye, F.; Liang, H.; Shi, A.C. Effect of polydispersity on the formation of vesicles from amphiphilic diblock copolymers. *Macromolecules* **2005**, *38*, 6710–6717. [[CrossRef](#)]
21. Gavrilov, A.A.; Shupanov, R.M.; Chertovich, A.V. Phase Diagram for Ideal Diblock-Copolymer Micelles Compared to Polymerization-Induced Self Assembly. *Polymers* **2020**, *12*, 2599. [[CrossRef](#)]
22. Huang, F.; Lv, Y.; Wang, L.; Xu, P.; Lin, J.; Lin, S. An insight into polymerization-induced self-assembly by dissipative particle dynamics simulation. *Soft Matter* **2016**, *12*, 6422–6429. [[CrossRef](#)]
23. Yan, Y.D.; Xue, Y.H.; Zhao, H.Y.; Liu, H.; Lu, Z.Y.; Gu, F.L. Insight into the Polymerization-Induced Self-Assembly via a Realistic Computer Simulation Strategy. *Macromolecules* **2019**, *52*, 6169–6180. [[CrossRef](#)]
24. Wang, J.; Fang, T.; Li, J.; Yan, Y.; Li, Z.; Zhang, J. Precise Mesoscopic Model Providing Insights into Polymerization-Induced Self-Assembly. *Langmuir* **2020**, *36*, 8009–8016. [[CrossRef](#)] [[PubMed](#)]
25. Lv, Y.; Wang, L.; Liu, F.; Feng, W.; Wei, J.; Lin, S. Rod-coil block copolymer aggregates via polymerization-induced self-assembly. *Soft Matter* **2020**, *16*, 3466–3475. [[CrossRef](#)] [[PubMed](#)]
26. Hoogerbrugge, P.J.; Koelman, J.M.V.A. Simulating Microscopic Hydrodynamic Phenomena with Dissipative Particle Dynamics. *Europhys. Lett. (EPL)* **1992**, *19*, 155–160. [[CrossRef](#)]
27. Koelman, J.M.V.A.; Hoogerbrugge, P.J. Dynamic Simulations of Hard-Sphere Suspensions Under Steady Shear. *Europhys. Lett. (EPL)* **1993**, *21*, 363–368. [[CrossRef](#)]
28. Schlijper, A.G.; Hoogerbrugge, P.J.; Manke, C.W. Computer simulation of dilute polymer solutions with the dissipative particle dynamics method. *J. Rheol.* **1995**, *39*, 567–579. [[CrossRef](#)]
29. Español, P.; Warren, P. Statistical Mechanics of Dissipative Particle Dynamics. *Europhys. Lett. (EPL)* **1995**, *30*, 191–196. [[CrossRef](#)]
30. Groot, R.D.; Warren, P.B. Dissipative particle dynamics: Bridging the gap between atomistic and mesoscopic simulation. *J. Chem. Phys.* **1997**, *107*, 4423–4435. [[CrossRef](#)]
31. Blanazs, A.; Ryan, A.; Armes, S. Predictive phase diagrams for RAFT aqueous dispersion polymerization: Effect of block copolymer composition, molecular weight, and copolymer concentration. *Macromolecules* **2012**, *45*, 5099–5107. [[CrossRef](#)]
32. Gavrilov, A.A.; Chertovich, A.V. Copolymerization of partly incompatible monomers: An insight from computer simulations. *Macromolecules* **2017**, *50*, 4677–4685. [[CrossRef](#)]
33. Tan, J.; Bai, Y.; Zhang, X.; Zhang, L. Room temperature synthesis of poly (poly (ethylene glycol) methyl ether methacrylate)-based diblock copolymer nano-objects via Photoinitiated Polymerization-Induced Self-Assembly (Photo-PISA). *Polym. Chem.* **2016**, *7*, 2372–2380. [[CrossRef](#)]
34. Wang, G.; Wang, Z.; Lee, B.; Yuan, R.; Lu, Z.; Yan, J.; Pan, X.; Song, Y.; Bockstaller, M.R.; Matyjaszewski, K. Polymerization-induced self-assembly of acrylonitrile via ICAR ATRP. *Polymer* **2017**, *129*, 57–67. [[CrossRef](#)]

35. Zhao, D.; Ma, Y.; Wang, E.; Lodge, T.P. Micellization of Binary Diblock Co-polymer Mixtures in an Ionic Liquid. *Macromolecules* **2019**, *52*, 4729–4738. [[CrossRef](#)]
36. Wang, Y.; Han, G.; Duan, W.; Zhang, W. ICAR ATRP in PEG with Low Concentration of Cu (II) Catalyst: A Versatile Method for Synthesis of Block Copolymer Nanoassemblies under Dispersion Polymerization. *Macromol. Rapid Commun.* **2019**, *40*, 1800140. [[CrossRef](#)]
37. Genzer, J. In silico polymerization: Computer simulation of controlled radical polymerization in bulk and on flat surfaces. *Macromolecules* **2006**, *39*, 7157–7169. [[CrossRef](#)]